Plastin increases cortical connectivity to facilitate robust polarization and timely cytokinesis

Wei Yung Ding,[1] Hui Ting Ong,[1] Yusuke Hara,[1,2] Jantana Wongsantichon,[3] Yusuke Toyama,[1,2,4] Robert C. Robinson,[3,5] François Nédélec,[6] and Ronen Zaidel-Bar[1,7]

[1]Mechanobiology Institute, National University of Singapore, Singapore 117411, Singapore
[2]Temasek Life Sciences Laboratory, 1 Research Link, National University of Singapore, Singapore 117604, Singapore
[3]Institute of Molecular and Cell Biology, A*STAR (Agency for Science, Technology, and Research), Singapore 138673, Singapore
[4]Department of Biological Sciences, National University of Singapore, Singapore 117543, Singapore
[5]Department of Biochemistry, National University of Singapore, Singapore 117597, Singapore
[6]Cell Biology and Biophysics Unit, European Molecular Biology Laboratory, 69117 Heidelberg, Germany
[7]Department of Biomedical Engineering, Faculty of Engineering, National University of Singapore, Singapore 117583, Singapore

The cell cortex is essential to maintain animal cell shape, and contractile forces generated within it by nonmuscle myosin II (NMY-2) drive cellular morphogenetic processes such as cytokinesis. The role of actin cross-linking proteins in cortical dynamics is still incompletely understood. Here, we show that the evolutionarily conserved actin bundling/cross-linking protein plastin is instrumental for the generation of potent cortical actomyosin contractility in the *Caenorhabditis elegans* zygote. PLST-1 was enriched in contractile structures and was required for effective coalescence of NMY-2 filaments into large contractile foci and for long-range coordinated contractility in the cortex. In the absence of PLST-1, polarization was compromised, cytokinesis was delayed or failed, and 50% of embryos died during development. Moreover, mathematical modeling showed that an optimal amount of bundling agents enhanced the ability of a network to contract. We propose that by increasing the connectivity of the F-actin meshwork, plastin enables the cortex to generate stronger and more coordinated forces to accomplish cellular morphogenesis.

Introduction

Actomyosin-mediated cortical contractility is essential for a large number of force-dependent biological processes, from polarization and cytokinesis at the single-cell level to wound healing and embryo morphogenesis at the multicellular level (Maddox et al., 2005; Lecuit and Lenne, 2007; Levayer and Lecuit, 2012; Salbreux et al., 2012; Munjal and Lecuit, 2014; Zaidel-Bar et al., 2015). The cortex in these processes undergoes constant remodeling and is capable of forming complex higher-order structures (Stossel et al., 2006; Tse et al., 2011). Such structural plasticity is made possible by the capability of actin to be polymerized and depolymerized, bundled and cross-linked, and anchored to the plasma membrane by a multitude of actin-binding proteins (Skop et al., 2004; Salbreux et al., 2012; Fievet et al., 2013). Although the role of F-actin cross-linking proteins has been extensively studied in vitro (Wachsstock et al., 1994; Gardel et al., 2004; Delanote et al., 2005; Wagner et al., 2006; Murrell and Gardel, 2012), their function in the cortex of animal cells is still poorly understood. As such, our goal in this study was to address how cross-linking affects the architecture of the cortex and its capacity to drive contractility-dependent processes in vivo.

The *Caenorhabditis elegans* zygote is an excellent model to investigate this question as important developmental processes such as polar body extrusion, polarization, and the first cell division depend on cortical contractility. Cortical actomyosin in early *C. elegans* embryos consists of a network of nonmuscle myosin II (NMY-2) foci interconnected by F-actin bundles (Strome, 1986; Lin et al., 1993; Munro et al., 2004; Dimitriadi et al., 2010). Asymmetric contractility within the cortex results in cortical flows that initiate polarization when directed from posterior to anterior and chirality when the flow is rotational (Hird and White, 1993; Munro et al., 2004; Mayer et al., 2010; Naganathan et al., 2014; Schonegg et al., 2014). Cortical dynamics are also responsible for cytokinetic ring formation and cell division (Werner et al., 2007), and are regulated by non-junctional HMR-1/E-cadherin clusters (Padmanabhan et al., 2017).

Plastin (also know as fimbrin) orthologues can be found from lower eukaryotes to humans (Delanote et al., 2005). Mammals have three plastin genes, two of which are tissue specific and one of which is expressed ubiquitously, whereas invertebrates, including *C. elegans*, have only one plastin gene (Strome, 1986;

Correspondence to Ronen Zaidel-Bar: zaidelbar@gmail.com

Abbreviations used: A-P, anterior–posterior; CH, calponin homology; D-V, dorsal–ventral axis; NMY-2, nonmuscle myosin II; PIV, particle image velocimetry.

Lin et al., 1993; Munro et al., 2004; Dimitriadi et al., 2010). The canonical structure of plastin consists of a headpiece made up of two EF-hands, followed by two actin-binding domains, each comprising two calponin homology (CH) domains (de Arruda et al., 1990). Plastin is a globular protein that can assemble F-actin into tightly packed bundles in parallel or antiparallel orientation (Bretscher, 1981; Glenney et al., 1981; Matsudaira et al., 1983; Skau et al., 2011). Plastin isoforms in vertebrates have been shown to associate with F-actin in intestinal microvilli, cochlear stereocilia, immune synapses, and podosomes (Bretscher and Weber, 1980; Flock et al., 1982; Messier et al., 1993; Wabnitz et al., 2010; Krey et al., 2016). A role for plastin in the cortex has been previously described in unicellular organisms. In *Tetrahymena thermophila*, plastin is found to localize to the furrowing cortex of the dividing cell (Shirayama and Numata, 2003). In *Dictyostelium discoideum*, plastin localizes to actin-rich cortical patches and resists NMY-2–dependent furrow ingression (Prassler et al., 1997; Reichl et al., 2008). In *Schizosaccharomyces pombe*, plastin cooperates with another actin cross-linking protein, α-actinin, to regulate internodal spacing for normal cytokinetic ring formation (Laporte et al., 2012). Although previous results of high-throughput RNAi screens conducted in *C. elegans* suggested that the plastin orthologue PLST-1 plays a role in polarization and cytokinesis (Skop et al., 2004; Fievet et al., 2013), its function in regulating cortical contractility during early embryogenesis has not been elucidated.

Results

PLST-1 associates with both formin- and arp2/3-mediated cortical F-actin and is enriched in contractile structures

Sequence analysis of the *C. elegans* genome revealed that PLST-1 is the only full-length protein having extensive conservation with other metazoans' plastin/fimbrin (Fig. S1). RT-PCR analysis revealed two possible isoforms of PLST-1, different by only three amino acids in the unstructured region between the second and third CH domains (Fig. S1, cyan arrowheads). The two isoforms shared >47% identity and >62% similarity with all three human plastin isoforms (PLS1, PLS2, and PLS3). We noted that residues critical for calcium binding in the EF-hands were not conserved in *C. elegans* PLST-1 (Fig. S1, red arrowheads). Also, the serine residue that was previously shown to be phosphoregulated in human PLS2 appeared not to be conserved in PLST-1 (Fig. S1, green arrowhead; Messier et al., 1993).

To visualize the localization of endogenous PLST-1, we generated a translational fusion of PLST-1 with GFP at the C terminus using CRISPR/Cas9. PLST-1::GFP localized to both filamentous and punctate structures at the cortex of newly fertilized zygotes (Fig. 1 A, red and yellow arrowheads, respectively). PLST-1::GFP continued to be expressed ubiquitously during the first 5 h of embryogenesis, with prominent enrichment at cell–cell contacts (Fig. S2 A, red arrowheads), and during elongation, PLST-1::GFP was enriched in the buccal region of the epidermis (Fig. S2 A, cyan arrowhead), pharynx (Fig. S2 A, green arrowhead), and intestine (Fig. S2 A, magenta arrowhead). We also noted that PLST-1 was expressed in various cells in the adult hermaphrodite, as shown in Fig. S2 B.

The filamentous and punctate structures formed by PLST-1::GFP in the newly fertilized zygote were also labeled by Lifeact::RFP, an F-actin reporter (Fig. 1 A and Video 1). The strong colocalization of the PLST-1::GFP and Lifeact::RFP signals, from before polarization, during polarity establishment and maintenance, and throughout cytokinesis, is evident in the representative line scans (Fig. 1 A) and from calculated Pearson's correlation coefficients with values >0.7 ($n \geq 8$; Fig. 1 B). This suggests that PLST-1::GFP associates with all cortical F-actin.

Previously, it has been shown that filamentous and punctate F-actin structures in the *C. elegans* zygote are assembled by two distinct nucleators: the diaphanous-like formin CYK-1 is responsible for filamentous structures, whereas the arp2/3 complex ARX-2/3 is responsible for punctate structures (Velarde et al., 2007; Shivas and Skop, 2012). To establish whether PLST-1 associates with F-actin polymerized by both nucleators, we examined PLST-1 localization in zygotes depleted for either *arx-2* or *cyk-1*. As expected, *arx-2(RNAi)* zygotes lost all puncta and retained only filamentous structures, whereas *cyk-1(RNAi)* zygotes lost the majority of filamentous structures and retained mostly puncta (Fig. 1 C). Importantly, PLST-1::GFP was observed to localize in the remaining structures under both conditions (Fig. 1 C), indicating that PLST-1 associates with both arp2/3- and formin-polymerized F-actin.

Although PLST-1 colocalized with all Lifeact-labeled F-actin structures, a closer examination of the fluorescence intensity profiles revealed that PLST-1 was particularly enriched (relative to Lifeact) at certain regions, most notably at the pseudocleavage and cytokinetic ring (Fig. 1 A, bottom panel). Ratiometric analysis further highlighted enrichment of PLST-1 in the aforementioned contractile structures, as well as actomyosin foci formed during polarity establishment (Fig. 1 D and Video 2). To gain insight into the dynamics of PLST-1 enrichment in F-actin foci, we followed both proteins throughout the lifetime of individual foci with high temporal resolution (Fig. 1 E). PLST-1 first appeared together with a loose network of F-actin, and as this network coalesced, the intensities of both F-actin and PLST-1 increased, but the intensity of PLST-1 increased more rapidly, leading to an enrichment of PLST-1 in the resulting focus. A further enrichment of PLST-1 occurred during the early stages of focus disassembly when the level of F-actin diminished faster than that of PLST-1.

PLST-1 binds and bundles F-actin in vitro

Plastin orthologues in a variety of organisms have been shown to bundle F-actin (Bretscher, 1981; Nakano et al., 2001; Shirayama and Numata, 2003; Skau et al., 2011). The high degree of protein similarity and the colocalization between PLST-1 and F-actin we observed during various stages of early embryogenesis suggested that *C. elegans* PLST-1 is also capable of bundling F-actin. To demonstrate this directly, we purified recombinant PLST-1 from *Escherichia coli* and used it in high-speed (150,000 *g*) or low-speed (14,000 *g*) F-actin cosedimentation experiments to test for F-actin binding or bundling activity, respectively (Fig. 2, A and B). In control experiments, high-speed centrifugation is unable to pellet PLST-1 in the absence of F-actin. However, when F-actin was introduced at increasing concentrations from 1 µM to 10 µM, the amount of PLST-1 pelleted together with F-actin increased as well (Fig. 2 A). This demonstrated that PLST-1 directly binds F-actin.

At low centrifugation speeds, only a small fraction of F-actin sedimented on its own. Addition of BSA did not change the proportion of sedimented F-actin. However, addition of PLST-1 lead to a massive shift of F-actin from the supernatant to the pellet, similar to the effect of adding recombinant
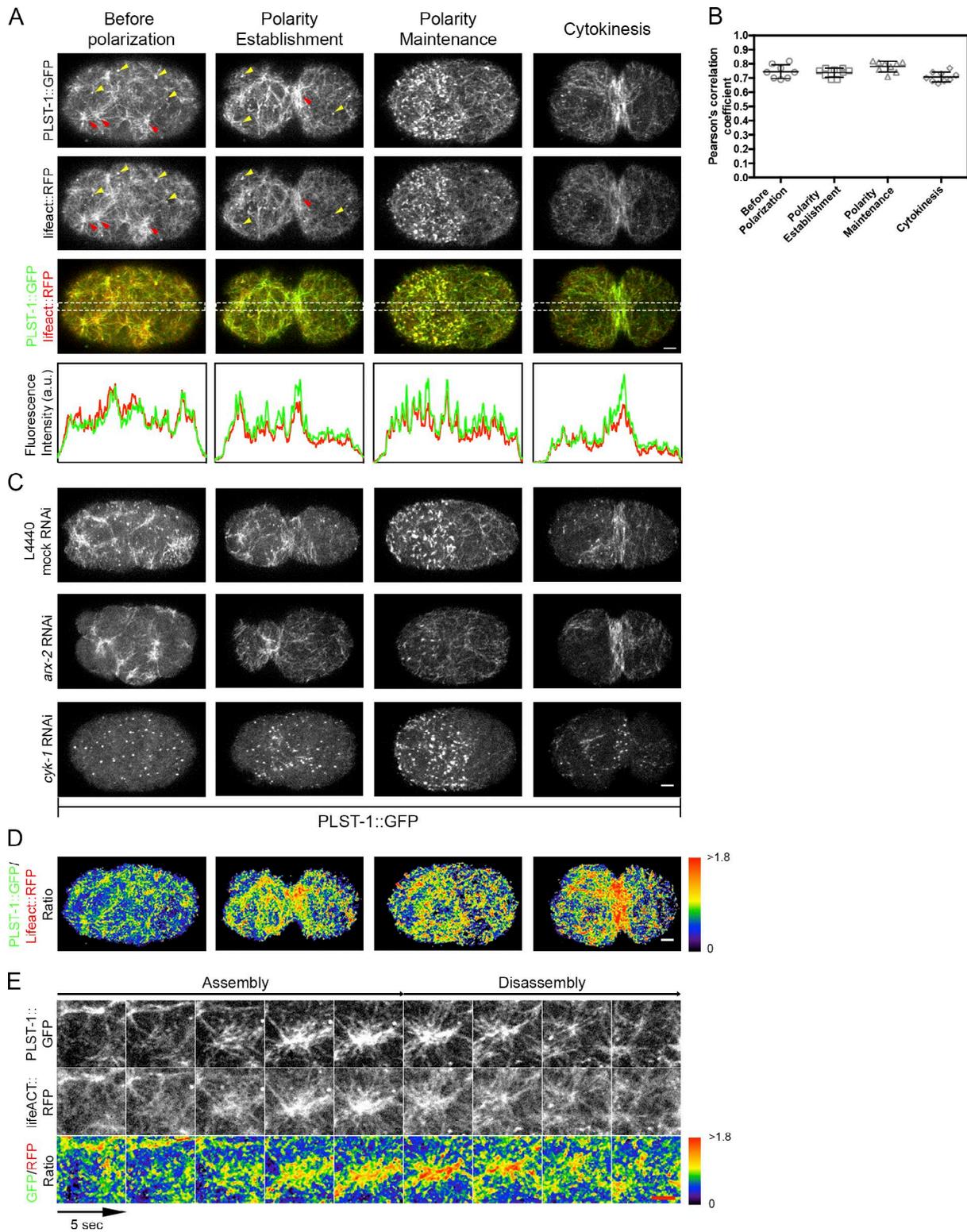
Figure 1. **Endogenous PLST-1 labeled with GFP localizes to the cortex of newly fertilized *C. elegans* zygotes.** (A) Cortical view of the newly fertilized *C. elegans* zygote coexpressing PLST-1::GFP and the F-actin reporter Lifeact::RFP. Punctate and filamentous structures are highlighted by yellow and red arrowheads, respectively. Colocalization of the PLST-1::GFP and Lifeact::RFP signals is shown in the merged channel and representative band scans. (B) Pearson's correlation between PLST-1::GFP and Lifeact::RFP at various stages in single-cell zygote ($n \geq 8$). (C) Filamentous and punctate structures formed by PLST-1::GFP can be separated by *arx-2* and *cyk-1* RNAi. (D) Ratiometric analysis of PLST-1::GFP/Lifeact::RFP fluorescent intensities reveals that PLST-1::GFP signal is enriched in contractile structures. (E) Time lapse of PLST-1::GFP/Lifeact::RFP during the formation and the subsequent disassembly of a contractile F-actin cluster during polarity establishment. Data are represented as mean ± SEM. Bars, 5 μm.

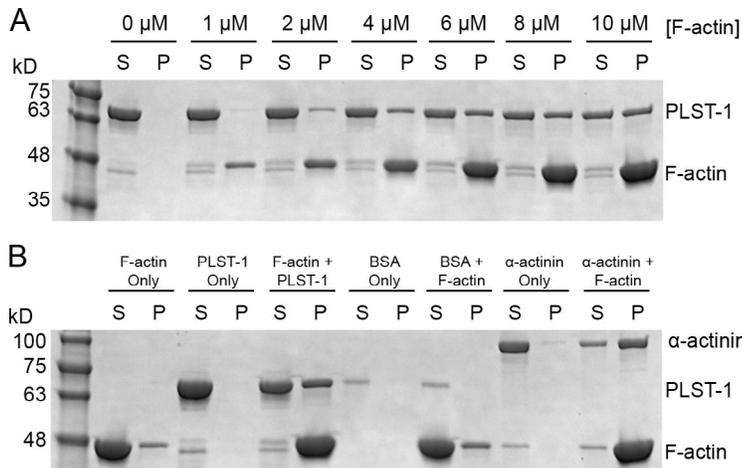Figure 2. **Recombinant PLST-1 binds and bundles F-actin in vitro.** (A) High-speed (150,000 g) F-actin cosedimentation assays were performed with recombinant PLST-1 at increasing F-actin concentrations. (B) Low-speed (14,000 g) F-actin cosedimentation assays were performed with recombinant PLST-1, α-actinin as a positive control, and BSA as a negative control. S, supernatant; P, pellet.

α-actinin (Fig. 2 B). F-actin will only pellet at low speed when bundled into higher-order supramolecular complexes (Meyer and Aebi, 1990). Thus, these results demonstrated that PLST-1 bundles F-actin in vitro.

Characterization of *plst-1(tm4255)* loss-of-function allele

To facilitate the study of PLST-1 function we made use of the *plst-1(tm4255)* allele, a 370-bp deletion mutant that abrogates most of the second-to-last exon encoding part of the third CH and most of the fourth CH domain (Fig. 3 A). To determine whether a truncated PLST-1 protein is being translated, we extracted mRNA and conducted RT-PCRs on both wild-type and *plst-1(tm4255)* mRNA. The *plst-1* mRNA amplicon was designed to begin at the start codon and stop 10 bp upstream of the *tm4255* deletion, allowing the detection of *plst-1* fragment cDNA if it were present in the mutant. Although we were able to detect *plst-1* cDNA in the control, *plst-1* cDNA (from the undeleted region) was undetectable in *plst-1(tm4255)* worms (Fig. 3 B), suggesting that the mRNA is unstable, likely because of nonsense-mediated decay (Behm-Ansmant et al., 2007; Chang et al., 2007), effectively rendering this a null mutant.

The *plst-1(tm4255)* allele resulted in 51% embryonic lethality ($n = 851$) compared with 0% in control embryos ($n = 850$). In contrast, *plst-1(RNAi),* which depleted PLST-1::GFP (Fig. S3 A), displayed only 11% embryonic lethality ($n = 340$). Although RNAi-mediated protein knockdown often results in a milder phenotype compared with a null mutant, this discrepancy could have also been caused by a second mutation in the *plst-1(tm4255)* strain that causes on its own an embryonic lethal phenotype and which is situated very close to the *plst-1* locus such that it cannot be crossed out. To rule out the latter possibility, we introduced via mos1-mediated single-copy insertion an additional copy of *plst-1::gfp* and tested its ability to rescue *plst-1(tm4255)* embryonic lethality (Fig. S3 B). We found the exogenous expression of PLST-1::GFP in the *plst-1(tm4255)* background eliminated embryonic lethality down to 0% ($n = 987$), confirming that all the embryonic lethality is caused by loss of plastin function. Hereafter, we refer to the *plst-1(tm4255)* allele as *plst-1*.

To establish the stage at which embryos failed to develop normally we followed embryogenesis of *plst-1* embryos in time-lapse Nomarski movies ($n = 41$). We found a range of terminal phenotypes: failure before gastrulation (22%), epidermal mor-

phogenesis failure (41%), and rupture during elongation (37%). Here, we focused on the earliest defects observed in the zygote.

plst-1 zygotes exhibit multiple abnormal phenotypes associated with reduced contractility

To follow events in early embryogenesis, we imaged newly fertilized zygotes coexpressing a membrane marker, GFP::PLC1δ-PH, and a histone marker, HIS-58::mCherry. As detailed in the following paragraphs, several cellular events attributed to actomyosin contractility were observed in the control zygotes but were severely attenuated in *plst-1* zygotes (Fig. 3 C and Video 3). Membrane ruffling, which occurred all around the control zygote, concurrent with the second meiosis, was strongly attenuated in *plst-1* zygotes (Fig. 3 C, yellow arrowheads). In control zygotes, the subsequent relaxation of the posterior cortex culminated in the formation of a pseudocleavage, marking the completion of polarity establishment. Pseudocleavage ingression depth was significantly attenuated in *plst-1* zygotes compared with the control ($2.4\% \pm 0.6\%$ vs. $40.3\% \pm 3.6\%$; $n \geq 13$; Fig. 3, C [red arrowheads] and D).

After polarity establishment, the oocyte and the sperm pronuclei meet. Consistent with a previous study, control pronuclei met at the posterior half of the zygote (0.679 ± 0.004; $n = 16$; Fig. 3 E; Albertson, 1984). In contrast, the pronuclei of *plst-1* met significantly closer to the midpoint of the anterior–posterior (A-P) axis (0.566 ± 0.009; $n = 19$; P < 0.0001), a phenotype typically associated with disruption of the actin cytoskeleton, even though pronuclear migration is known to be dependent on microtubule-related machinery (Strome and Wood, 1983; Hill and Strome, 1988).

After anaphase onset, concurrent with spindle oscillation, multiple membrane invaginations were observed in *plst-1* zygotes, primarily in the posterior cortex (38.4 ± 2.7 invaginations/embryo; $n = 20$), whereas such invaginations were seldom observed in control zygotes (2.8 ± 0.5 invaginations/embryo; $n \geq 13$; Fig. 3, C [cyan arrowheads] and F). Such membrane invaginations were previously shown to result from the inability of the actomyosin cortex to resist pulling forces exerted by microtubules on the plasma membrane during spindle oscillation (Redemann et al., 2010). To demonstrate that this was the case here, we imaged *plst-1* zygotes coexpressing GFP::tubulin and PH::mCherry (Fig. 3 G and Video 4). We found that the tip of each membrane invagination in the posterior cortex of *plst-1* zygotes colocalized with a microtubule tip, consistent with the
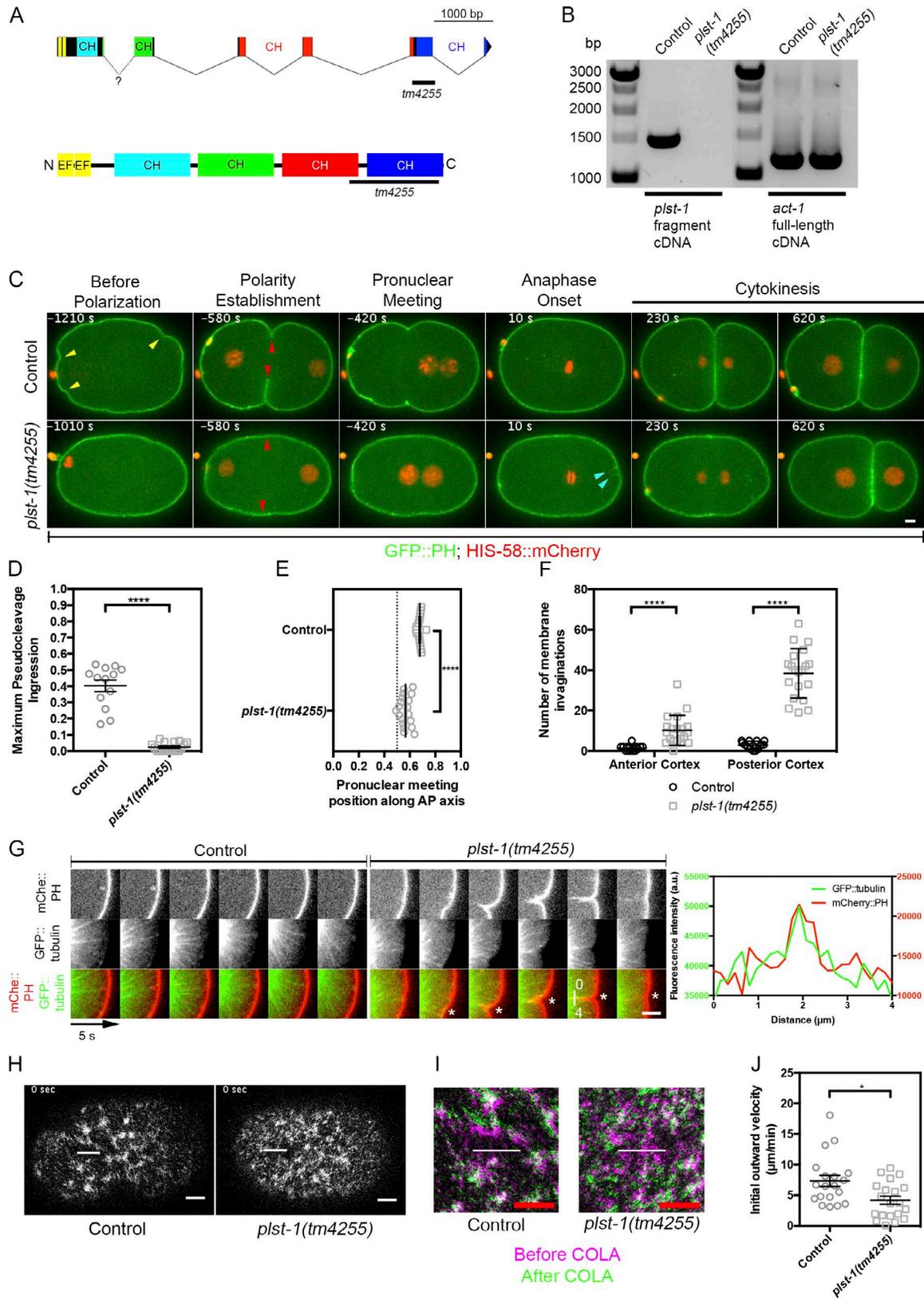
Figure 3. **plst-1 null zygotes display defects in cortical contractility-related processes during early embryogenesis.** (A) Schematic showing position of the *tm4255* deletion in the *plst-1* gene and its possible truncated protein product. CH, calponin homology domain; EF, EF-hand like domain. (B) RT-PCR analysis of *plst-1* mRNA in control and *plst-1(tm4255)* worms shows that no message can be detected in the mutant. (C) Equatorial view of control and *plst-1* zygotes expressing membrane marker GFP::PLC1δ-PH and histone marker HIS-58::mCherry. Yellow, red, and cyan arrowheads highlight cortical ruffling, pseudocleavage, and membrane invaginations, respectively. (D) Quantification of maximum pseudocleavage ingression in control (*n* = 13) and *plst-1* (*n* = 18) zygotes. (E) Quantification of pronuclear meeting position along the anterior–posterior (AP) axis in control (*n* = 16) and *plst-1* (*n* = 19) zygotes.

idea that plasma membrane invaginations were being pulled by microtubules (Fig. 3 G).

We repeated the phenotypic analysis with *plst-1(RNAi)* zygotes and observed similar attenuated contractility phenotypes only milder (Fig. S3 A). Importantly, all of the aforementioned phenotypes were completely rescued by expression of PLST-1::GFP in the *plst-1* background (Fig. S3, B–E). We investigated whether *plst-1* heterozygotes have any discernable phenotypes and found that they behave similarly to the wild-type, such as in the furrow closure time (248 ± 6 s vs. 232 ± 7 s; $n \geq 16$; P = 0.0965).

We also tested whether α-actinin played a similar role to *plst-1* in regulating early embryogenesis as a previous screen conducted in *C. elegans* found that the knockdown of *atn-1*, the worm orthologue of α-actinin, resulted in an early cytokinesis defect (Skop et al., 2004). However, we could not observe any loss of contractility phenotype in null mutant *atn-1(ok84)* zygotes (Fig. S4, A and B; Moulder et al., 2010) or enhancement of *plst-1* phenotype in *plst-1(tm4255);atn(ok84)* double mutant zygotes (Fig. S4, C and D).

The observation of membrane invaginations in the *plst-1* zygotes indicated that the cortex was not able to resist the microtubule-mediated pulling forces, suggesting the cortex in *plst-1* embryos is "weaker" or "softer," because of a change in tension and/or its mechanical properties. To test this hypothesis directly, we performed cortical laser ablations in control and *plst-1* zygotes expressing NMY-2::GFP when the anterior myosin-rich cortex occupied 70% of the embryo length (Fig. 3 H). The initial recoil velocity measured in the *plst-1* zygotes was significantly lower compared with that of the control (4.17 ± 0.67 μm/min vs. 7.35 ± 0.92 μm/min; $n \geq 19$; P < 0.05; Fig. 3 I and Video 5). These results demonstrate directly that cortical mechanics are disrupted by *plst-1* loss of function.

PLST-1 is required for effective coalescence of nascent NMY-2 filaments into mature contractile foci

Given the loss of cortical contractility phenotype in *plst-1* zygotes, we compared the structural organization of the cortical actomyosin network between control and *plst-1* zygotes. We imaged GFP::Utrophin and NMY-2::mCherry at the cortex before, during, and after the establishment of polarity (Fig. 4 A). The appearance of F-actin bundles was similar in control and *plst-1* zygotes. Quantification of fluorescence intensities of GFP::Utrophin and NMY-2::mCherry throughout the establishment of polarity showed no difference between control and *plst-1* (Fig. S5 A), suggesting that PLST-1 does not regulate cortical contractility through the recruitment of F-actin or NMY-2.

However, the cortical distribution of NMY-2 was noticeably different: whereas in control zygotes NMY-2 was mainly concentrated in a small number of large foci, in *plst-1* zygotes, NMY-2 was dispersed throughout the cortex and formed mostly small foci, suggesting that NMY-2 is unable to coalesce into large and mature foci in *plst-1* zygotes (Fig. 4 A).

Previous work has shown that NMY-2 foci form through coalescence of smaller nascent NMY-2 filaments (Munro et al., 2004). We reasoned that the smaller NMY-2 foci in *plst-1* zygotes could be the result of diminished coalescence because of the lack of cross-linking activity in the network. To test this hypothesis, we chose mature NMY-2 foci observed in time-lapse movies of control and *plst-1* polarizing zygotes and traced their formations from smaller nascent NMY-2 filaments (Fig. 4 B). As expected, in both control and *plst-1* zygotes, the formation of a mature NMY-2 focus was often preceded by visible coalescence of smaller NMY-2 filaments from a region surrounding the eventual focus. There was, however, a pronounced difference between control and *plst-1* in the area participating in the coalescence process. Quantification confirmed the median cortical area of interacting nascent NMY-2 filaments in control was larger compared with *plst-1* zygotes (9.93 μm² vs. 7.07 μm²; $n \geq 110$; $n \geq 11$; Fig. 4 C). Quantification also determined that the median mature NMY-2 focus area in control was twofold larger compared with *plst-1* zygotes (4.40 μm² vs. 2.13 μm²; $n \geq 236$; $n \geq 10$; Fig. 4 D).

During the analysis of foci dynamics, we noted that once assembled, NMY-2 foci appeared to remain longer at the cortex in control zygotes compared with *plst-1* (Fig. 4 B). Quantification of the lifetime of NMY-2 foci during the establishment of polarity showed that the NMY-2 median foci lifetime in control zygotes was slightly longer than foci in *plst-1* zygotes (35 vs. 30 s; $n \geq 858$; $n = 9$; Fig. 4 E).

PLST-1 is required for long-range directional cortical flows

Next, we examined cortical dynamics in control and *plst-1* zygotes expressing GFP::Utrophin and NMY-2::GFP (Videos 6 and 7). In control zygotes, during polarity establishment, both actin and myosin displayed strong cortical flows from the posterior toward the anterior, as described previously (Munro et al., 2004). In contrast, *plst-1* zygotes displayed only weak cortical flows. This is evident in the kymographs shown in Fig. 5 A.

To further characterize cortical flows, we applied particle image velocimetry (PIV) analysis to the first 250 s of NMY-2::mCherry movies and generated mean velocity fields for both control and *plst-1* zygotes (Fig. 5 B). These velocity fields clearly showed that flow in the *plst-1* mutant is not only weaker but also less coherent in its direction. A plot of the mean velocity profile along the A-P axis during polarization shows the flow in control zygotes to be significantly higher than in the *plst-1* zygotes all along the A-P axis (Fig. 5 C; and Fig. S5, B and C), confirming that PLST-1 activity is required for the generation of strong cortical flows.

To quantify directional persistence in cortical flows, we measured the cosine similarity between two vectors (defined as the cosine of the angle subtended by the two vectors) and plot-

---

Dotted line represents medial position (i.e., 0.5) along the A-P axis. (F) Quantification of the number of membrane invaginations in the anterior and posterior cortex of the control (*n* = 13) and *plst-1* (*n* = 20) zygotes from anaphase onset to cytokinesis completion. (G) Montages of the posterior cortex in control and *plst-1* zygotes expressing mCherry::PLC1δ-PH and GFP::tubulin during spindle oscillation. Asterisks indicate sites of membrane invaginations. Representative line scan of mCherry::PLC1δ-PH and GFP::tubulin signals in the *plst-1* montage are shown on the right. (H) Cortical view of control and *plst-1* zygotes expressing NMY-2::GFP with laser ablation being performed at the anterior cortex. White line depicts site of ablation. (I) Superimposed images of NMY-2::GFP before (magenta, −5 s) and after (green, +5 s) cortical laser ablation (0 s) in control and *plst-1* zygotes. White line depicts site of ablation. (J) Quantification of initial outward velocity after cortical laser ablation in control (*n* = 19) and *plst-1* (*n* = 20) zygotes. Data are represented as mean ± SEM. ****, P < 0.0001; *, P < 0.05; Mann–Whitney *U* test. Bars, 5 μm.
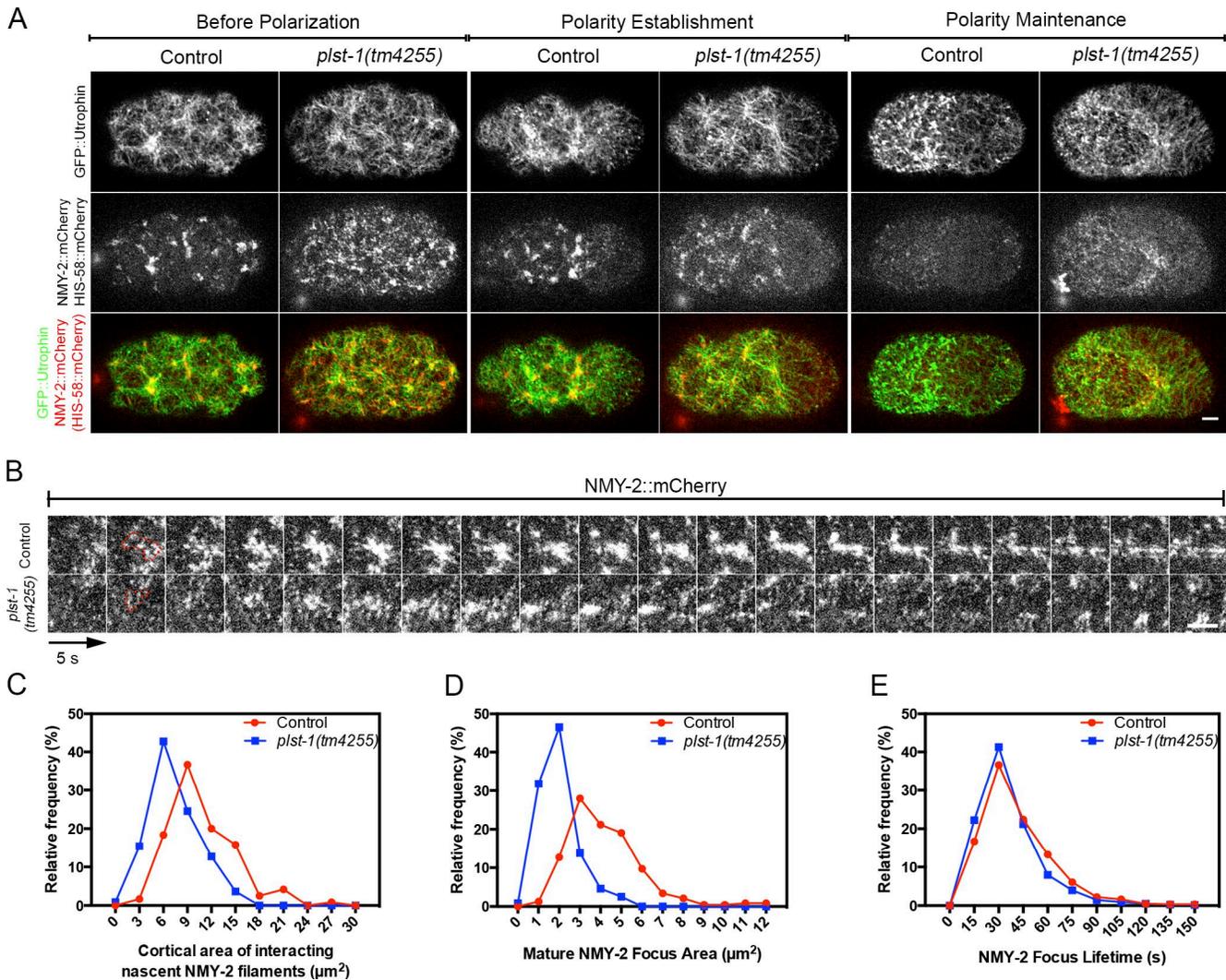
Figure 4. **PLST-1 is essential for effective coalescence of nascent NMY-2 filaments into mature contractile foci.** (A) Cortical views of control and *plst-1* zygotes coexpressing GFP::Utrophin, NMY-2::mCherry, and HIS-58::mCherry before, during, and after polarization. Bar, 5 µm. (B) Time-lapse montage of the formation and the subsequent disassembly of an NMY-2 focus during polarity establishment in control and *plst-1* zygotes. Bar, 5 µm. (C) Histogram showing distribution of mature NMY-2 foci area in control (*n* = 10, *n* = 236) and *plst-1* (*n* = 10, *n* = 239) zygotes. (D) Histogram showing distribution of initial cortical area coalescing into NMY-2 foci in control (*n* = 14, *n* = 120) and *plst-1* (*n* = 11, *n* = 110) zygotes. (E) Histogram showing distribution of NMY-2 foci lifetime in control (*n* = 9, *n* = 858) and *plst-1* (*n* = 9, *n* = 1156) zygotes.

ted the mean cosine similarity against each separation distance between two vectors (Fig. 5 D). The cosine similarity in *plst-1* zygotes decayed much faster with distance than the control. The cosine similarity length (defined as the distance where the cosine similarity drops to zero) of the cortex in the control was approximately twofold longer than that of the *plst-1* zygotes (34.5 ± 1.4 µm vs. 17.6 ± 0.8 µm; $n \geq 14$; P < 0.001; Fig. 5 E). The same analysis conducted on GFP::Utrophin yielded the same conclusion (Fig. S5, D–G).

A second phase of cortical flow takes place concurrent with the formation of the cytokinetic ring, when the cortex undergoes a coordinated rotation followed by flows from the poles toward the ingression furrow (Video 8; Hird and White, 1993; Schonegg et al., 2014; Singh and Pohl, 2014). We analyzed cortical flow dynamics using PIV from anaphase onset until furrow ingression (Fig. S5 H). Our analysis showed that in control zygotes the cortex was relatively static for the initial 30 s, followed by strong rotational flow along the dorsal–ventral (D-V) axis, with the flow velocity peaking between 50 and 70 s at ~20 µm/min, and ended with cortical flows from the poles toward the ingression furrow (Fig. S5, I and J). In *plst-1* zygotes, on the other hand, strong erratic flows were observed in both the A-P axis and the D-V axis in both the anterior and posterior cortices for the first 90 s. The erratic flow in both cortices then transitioned into weak clockwise (viewed from the anterior pole) flow at the anterior cortex and strong counterclockwise flow at the posterior cortex. Such opposing flows in the anterior and posterior cortices persisted until the cytokinetic ring ingressed from the focal plane (Fig. S5, I and J).

We quantified the cosine similarity between two vectors against the distance between them during the period between anaphase onset and furrow ingression and found that the cosine similarity between two vectors decayed much faster in *plst-1* zygotes than in control zygotes (Fig. S5 K).

Collectively, these results suggest that PLST-1 increases the connectivity of the actomyosin network to facilitate long-range coordinated and persistent cortical flows.
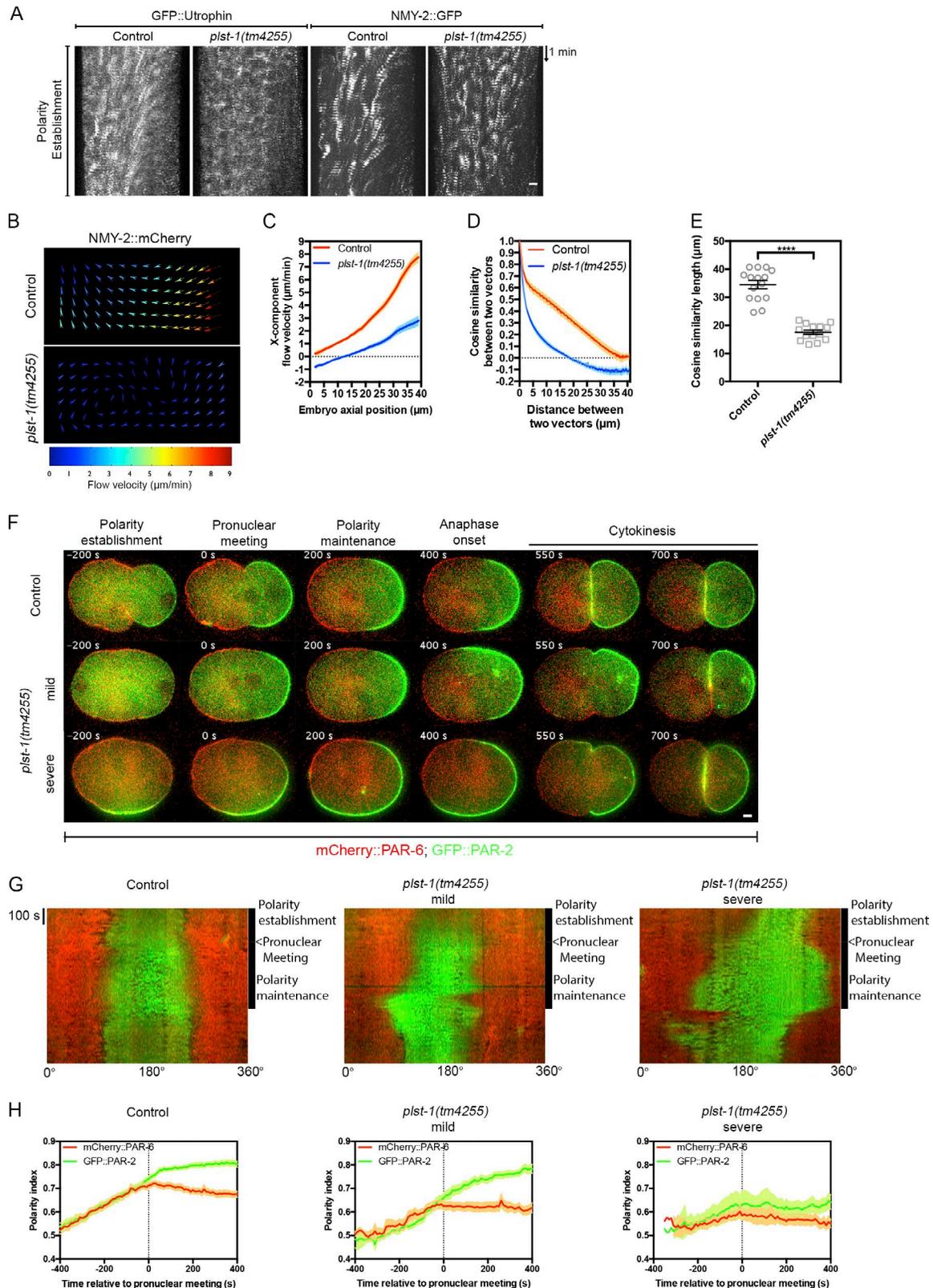
Figure 5. **PLST-1 is required for long-range directional cortical flows and robust polarization of the zygote.** (A) Representative kymographs of GFP::Utrophin and NMY-2::GFP in control and *plst-1* zygotes during polarity establishment and maintenance. (B) Mean vector field of NMY-2::mCherry cortical flow in the control (*n* = 6) and *plst-1* (*n* = 5) cortex during polarity establishment, based on PIV analysis. (C) X-component velocity profiles of NMY-2::mCherry cortical flow in control (*n* = 15) and *plst-1* (*n* = 14) zygotes during polarity establishment. (D) Decay profile of cosine similarity between 2 vectors in the NMY-2::mCherry cortical flow in control (*n* = 15) and *plst-1* zygotes (*n* = 14) during polarity establishment. (E) Cosine similarity length of control (*n* = 15) and *plst-1* (*n* = 14) zygotes during polarity establishment. Data are represented as mean ± SEM. ****, P < 0.0001, by Mann–Whitney *U* test. (F) Equatorial view of control, *plst-1* mild, and *plst-1* severe zygotes expressing mCherry::PAR-6 and GFP::PAR-2. Bars, 5 µm. (G) Representative kymographs

PAR protein segregation during polarity establishment is defective in *plst-1* zygotes

Because we observed a severe defect in actomyosin cortical flows during polarity establishment and a defect in polarization of the cortex, we wondered how plastin loss of function affects the polar distribution of the anterior and posterior PAR proteins, which is known to be, at least initially, dependent on cortical flow (Munro et al., 2004). To this end, we imaged zygotes expressing mCherry::PAR-6 and GFP::PAR-2 as markers for anterior and posterior PAR proteins, respectively, in both control and *plst-1* zygotes (in the *par-2(ok1723)* null background for visualization of PAR-2 dynamics at close to wild-type levels; Video 9). Time series from representative movies are shown in Fig. 5 F, and corresponding linearized membrane kymographs are shown in Fig. 5 G. The control embryos all showed the expected rapid segregation of PAR proteins during establishment of polarity, which was completed by the time the pronuclei met and thereafter remained stable. Among *plst-1* zygotes we distinguished two phenotypes in terms of severity. 78% of the *plst-1* zygotes ($n = 14$) displayed a mild phenotype, where the boundary established between mCherry::PAR-6 and GFP::PAR-2 was more posterior compared with the control (Fig. 5, F and G; *plst-1(tm4255)* mild). During anaphase onset, the boundary between anterior and posterior PAR domains was more volatile and eventually distorted in the divided zygote. In the remaining 22% of the *plst-1* zygotes ($n = 4$), severe distortion of the boundary was evident even before the establishment of polarity (Fig. 5, F and G; *plst-1(tm4255)* severe). Unlike its mild counterpart, the distorted GFP::PAR-2 domain increased in size and eventually encompassed more than the posterior cortex, overreaching into the anterior cortex during polarity maintenance. This boundary distortion corrected itself partially upon anaphase onset and the PAR proteins eventually segregated themselves into respective daughter cells.

We calculated a polarity index, which is a measure of the enrichment of each PAR protein in its respective domain relative to the entire cortex, and plotted it over time in control and both mutant groups (Fig. 5 H). This quantification confirmed that PAR protein segregation is defective during polarity establishment (-400 s to 0 s, relative to pronuclear meeting) in both mild and severe *plst-1* zygotes, and in the severe *plst-1* zygotes, polarity is not rescued even during polarity maintenance phase (Fig. 5 H).

PLST-1 promotes efficient recruitment of myosin for timely cytokinesis

After anaphase onset, the zygote cortex undergoes major remodeling, culminating in the formation of a cytokinetic ring that will ingress and divide the cell in two (Lewellyn et al., 2011). We have observed, using a plasma membrane marker, a substantial delay in cytokinesis in *plst-1* zygotes (Fig. 3 C). Further examination of a large number of *plst-1* embryos revealed the existence of three phenotypes: in 85% of zygotes, cytokinesis initiation was delayed but cytokinesis was eventually completed; in 6%, cytokinesis was delayed, and after it began, it regressed; and in 9%, cytokinesis initiation completely failed ($n = 34$; Fig. 6 A). We focused our analysis on the major phenotype (i.e., a delay in the initiation but completion of cytokinesis). Quantification confirmed that the time period from anaphase onset to the completion of cytokinesis in control zygotes was significantly shorter than that of *plst-1* zygotes that were able to complete cytokinesis (244 ± 4 s vs. 421 ± 10 s; $n \geq 18$; $P < 0.0001$; Fig. 6 B). A close examination of the dynamics of furrow ingression showed that the delay manifested primarily during the initiation phase (1.0 to 0.75 normalized cortical distance), and there was no significant difference in the furrow constriction rate during the ingression period (0.75 to 0 normalized cortical distance) between control zygotes and the 85% of *plst-1* zygotes (0.276 ± 0.017 µm/s vs. 0.254 ± 0.01 µm/s; $n \geq 13$; $P = 0.234$; Fig. 6, C and D) that completed cytokinesis. Combining these observations, we conclude that plastin loss of function results in 85% of zygotes in a pronounced delay in furrow initiation, and in 15% of zygotes, a defect in furrow ingression.

To gain molecular insight into the cause of the delay in cytokinesis initiation, we investigated actomyosin dynamics at the future furrowing site immediately after anaphase onset in zygotes coexpressing GFP::Utrophin, NMY-2::mCherry, and HIS-58::mCherry (Fig. 6 E and Video 8). We found distinct differences in F-actin and NMY-2 recruitment to the cytokinetic ring between control and *plst-1* zygotes. In control zygotes, F-actin and NMY-2 concurrently accumulated at the cytokinetic ring, peaking ~90 s after anaphase onset, after which furrow ingression led to a decrease in both F-actin and NMY-2 signals in the plane of observation (Fig. 6, E and F). In contrast, in *plst-1* zygotes, an initial increase in F-actin was shorter lived (peaked at 48 s), was not accompanied by NMY-2 recruitment, and did not result in furrow ingression. NMY-2 fluorescence levels remained flat until ~100 s after anaphase onset, after which they rose gradually, along with a second increase in F-actin levels, culminating in furrow ingression ~200 s after anaphase onset (Fig. 6 F). We conclude that PLST-1 promotes efficient recruitment of myosin for timely and robust cytokinetic ring formation.

In silico simulations and PLST-1 overexpression indicate there exists an optimal level of connectivity for effective contractility

To gain further insight into how the amount of F-actin cross-linking affects cortical contractility, we used Cytosim (Nédélec and Foethke, 2007) to simulate the behavior the cortex. We modeled a circular patch of cortex of radius 10 µm made up of filaments having the flexibility of F-actin, and we varied the amounts of motor and cross-linking proteins (Fig. 7 A). As expected, without motor proteins, the network did not contract or show any large-scale movement, with few or many cross-linkers (Fig. 7 A, first and second panels). Interestingly, in the presence of motors, but with relatively few cross-linkers, the network only contracted very slowly (Fig. 7 A, third panel). The optimal contraction rate was only reached when both motors and cross-linkers are abundant (Fig. 7 A, fourth panel). With our parameter set, the maximal contractility is obtained roughly at a 2:1 ratio. Interestingly, doubling or quadrupling
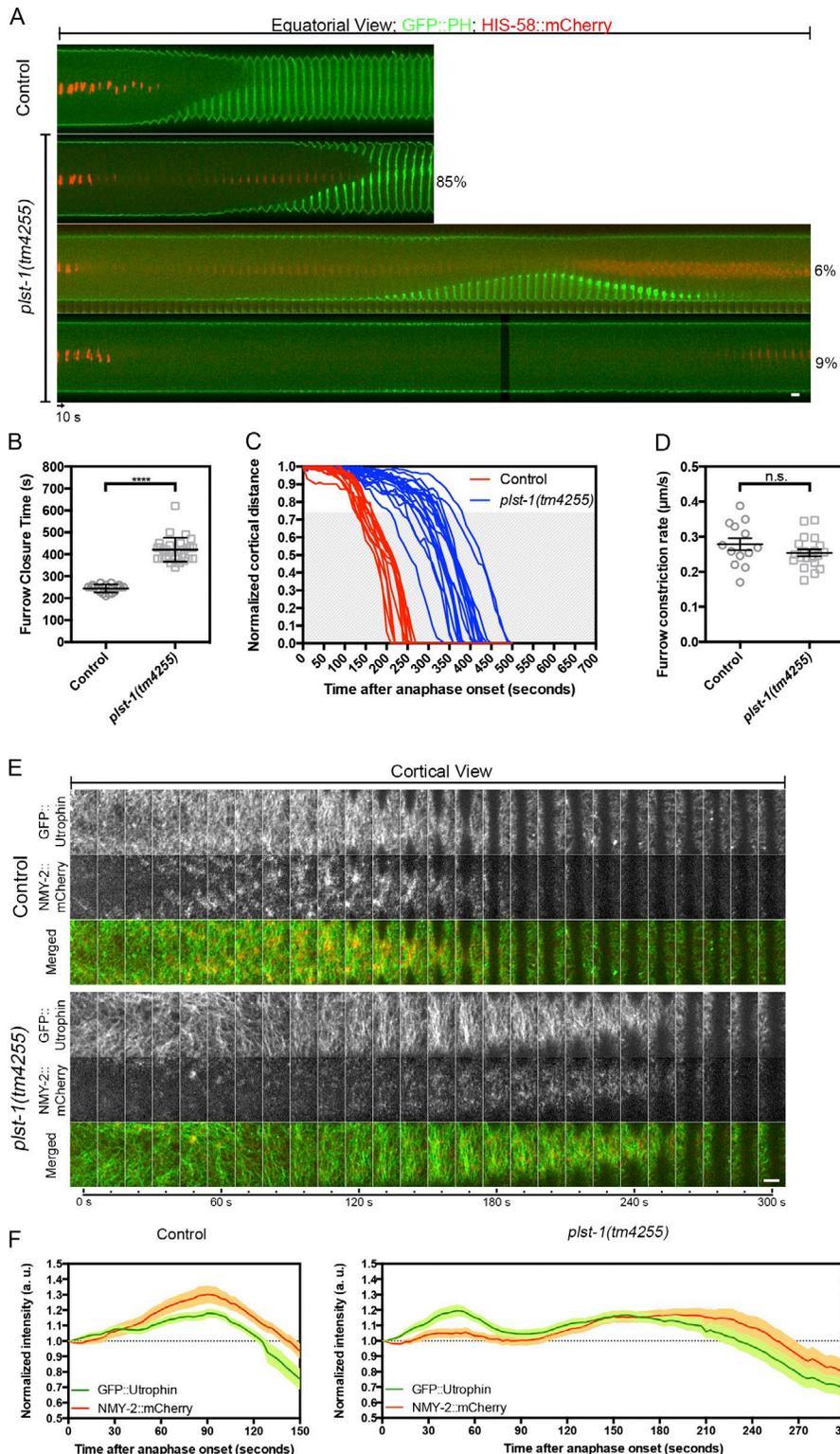
Figure 6. PLST-1 is needed for cytokinetic furrow formation, which requires concurrent recruitment of F-actin and myosin. (A) Time-lapse montages of equatorial segment of control and *plst-1* zygotes coexpressing GFP::PLC1δ-PH and HIS-58::mCherry from anaphase onset to the completion of cytokinesis. For all subsequent analyses of *plst-1* zygotes, measurements are only done on zygotes that are able to complete cytokinesis. (B) Quantification of time required from anaphase onset to the completion of cytokinesis in control (*n* = 18) and *plst-1* (*n* = 29) zygotes. (C) Furrowing kinetics of the control (*n* = 13) and *plst-1* (*n* = 20) zygotes from anaphase onset to the completion of cytokinesis. (D) Quantification of the furrow constriction rate from the normalized cortical distance of 0.75 to 0 (gray area in C) in control (*n* = 13) and *plst-1* (*n* = 20) zygotes. (E) Time-lapse montages of cortical segment of the furrow region in control and *plst-1* zygotes coexpressing GFP::Utrophin and NMY-2::mCherry from anaphase onset to complete ingression of the cortex from the imaged focal plane. (F) Normalized cortical fluorescence intensity profiles of GFP::Utrophin and NMY-2::mCherry in control (*n* = 16) and *plst-1* (*n* = 18) zygotes from anaphase onset to complete ingression of the cortex from focal plane. Data are represented as mean ± SEM. ****, P < 0.0001; n.s., not significant; Mann–Whitney *U* test. Bars, 5 µm.

the amount of cross-linker beyond this point reduced contractility significantly (Fig. 7 A, fifth and sixth panels). These results illustrate that the contractile rate depends on the amount of cross-linkers in a nonmonotonous manner: cross-linkers are necessary for contractility, but an excess of cross-linkers inhibits contractility.

The simulation predicted in particular that doubling the amount of cross-linker would have an inhibitory effect on con-

tractility. To test this prediction, we generated a strain expressing PLST-1::GFP driven by the *sip-1* promoter on top of endogenous PLST-1 driven by the endogenous *plst-1* promoter, resulting in excessive levels of PLST-1 at the cortex (Fig. 7 B). As an indicator for cortical contractility, we measured the time taken to complete cytokinesis from anaphase onset, and we found a significant increase in this time when PLST-1 is overexpressed (225 ± 5 s vs. 257 ± 8 s; *n* ≥ 16; P < 0.01), supporting the idea
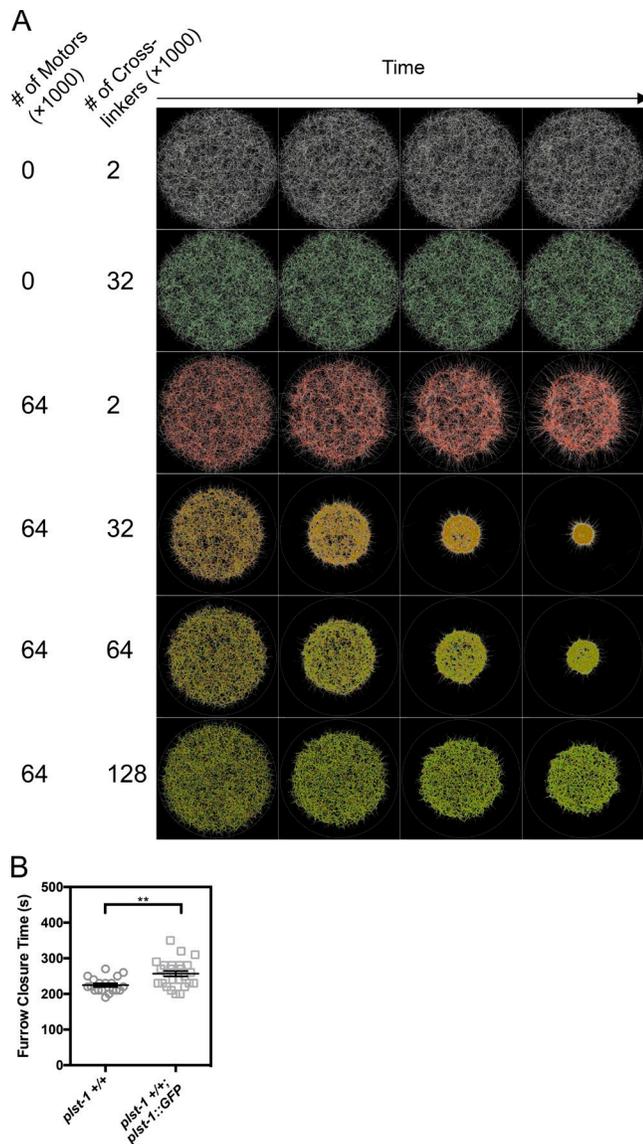
Figure 7. **Optimal amounts of cross-linker and motor activity are required for maximal actomyosin contraction in simulated and real cortex.** (A) Representative Cytosim simulations of the cortex with differing amount of motor and cross-linkers. From top to bottom, the number of motor/cross-linkers are: 0:2; 0:32; 64:2; 64:32; 64:64; 64:128 thousands. (B) Quantification of time required from anaphase onset to the completion of cytokinesis in control ($n = 19$) and *plst-1* overexpression ($n = 25$) zygotes. Data are represented as mean ± SEM. **, $P < 0.01$, by Mann–Whitney U test.

that there exists an optimal amount of PLST-1, above or below which cortical contractility is perturbed.

Discussion

Different plastin isoforms in vertebrates have been shown to be important for the function of microvilli in the intestinal brush border, stereocilia of the inner ear, and immune cell adhesion and migration (Flock et al., 1982; Ezzell et al., 1989; Wabnitz et al., 2010; Freeley et al., 2012). Plastin was also shown to be expressed in the mouse oocyte and early embryo, but its role there has not been studied (Ezzell et al., 1989). We found that the sole plastin orthologue in *C. elegans*, PLST-1, is also ex-

pressed in a variety of cells and tissues both in the adult and embryo, including strong localization in the intestine and in the cortex of all embryonic cells. In this paper, we focused on the role of PLST-1 in the cortex of the zygote. The *plst-1* null allele results in 51% embryonic lethality, but only 15% of zygotes were observed to fail in cytokinesis. It could be that failure in cytokinesis during later cell divisions explains the remaining embryonic lethality. However, it is also possible that PLST-1 function is required for additional developmental processes, such as epidermal morphogenesis.

Our results indicate that the presence of PLST-1 increases the stiffness of the cortex. This is evident in the response of the plasma membrane to pulling from within the cell by microtubules during spindle orientation and in the degree of cortical recoil in response to laser ablation. Normally, the cortex resists microtubule pulling forces, but in the *plst-1* zygotes, we observed numerous membrane invaginations being pulled through the cortex. Previously, it was shown that such invaginations occur when actin or myosin activity at the cortex is compromised (Redemann et al., 2010). Our results extend these observations to show that actin bundling activity also contributes to cortical stiffness, in line with findings from reconstituted cytoskeletal network studies (Xu et al., 1998).

How does PLST-1 augment cortical stiffness? Most likely, PLST-1 contributes in two ways: by increasing tension in the network and by modulating the mechanical properties of the actin gel. Limited by the resolution of confocal light microscopy, we were not able to distinguish nanoscale difference in the structure of control versus *plst-1* cortices. However, at the mesoscale, we could discern stark differences between the two, both in the size of NMY-2 foci and in their dynamics, from which we can deduce that PLST-1 is a major contributor to the connectivity of the cortical F-actin meshwork. Consistent with this idea, a recent in vitro study by Ennomani et al. (2016) showed that connectivity afforded by the actin cross-linking protein α-actinin to reconstituted actin rings modulates their contractility. In the worm, such connectivity facilitates coalescence and maturation of NMY-2 foci from distant nascent filaments, thereby permitting stronger cortical contractility. Similarly, Murrell and Gardel (2012) have described enlargement of the contractile domain in planar reconstituted actomyosin networks upon addition of the actin cross-linker α-actinin. Interestingly, we did not find any role for α-actinin in the early *C. elegans* zygote. Thus, it appears that F-actin bundling by PLST-1, along with NMY-2 cross-linking, is the major contributor to cortical connectivity in *C. elegans*.

The increased connectivity PLST-1 endows cortical actomyosin has far-reaching consequences for its large-scale dynamics. The contrast between the long-range and persistent cortical flows in control zygotes compared with the erratic and local flows observed in *plst-1* zygotes is dramatic. We were able to quantify the coordination along the cell cortex by measuring the cosine similarity length from PIV data (see Results) and found that during both polarity establishment and cytokinesis initiation, the cosine similarity length of *plst-1* zygotes was half of that in controls. Our in vivo results corroborate earlier work using in vitro reconstitution, where it has been demonstrated that a cross-linked F-actin meshwork can facilitate long-range myosin-mediated contraction (Janson et al., 1991; Bendix et al., 2008). Importantly, our work demonstrates that enhanced connectivity afforded by actin-bundling proteins is critically important in vivo for processes such as polarity establishment and cytokinesis.

Materials and methods

C. elegans strains maintenance

C. elegans strains were maintained using nematode growth medium plates seeded with *E. coli* strain OP50, as previously described (Brenner, 1974). All experiments were conducted at 20°C unless otherwise stated. Z. Bao (Memorial Sloan-Kettering Cancer Center, New York, NY) provided strain BU70 *[zbIs2(pie-1::lifeACT::RFP)]*. M. Glotzer (University of Chicago, Chicago, IL) provided strains MG511 *[ruIs57[pie-1::GFP::tubulin + unc-119(+)]; ltIs44[pAA173; pie-1::mCherry::PH(PLC1delta1); unc-119 (+)] V]* and MG589 *[mgSi3[cb-UNC-119 (+) GFP::UTROPHIN] II]*. A. Hart (Brown University, Providence, RI) provided a strain containing *plst-1(tm4255) IV* that had been backcrossed four times. F. Motegi (National University of Singapore, Singapore) provided strain MOT121 *[axIs1933[pFM034; GFP::par-2 RNAi-resistant (WT par-2 amount)]; temIs17[mCherry::PAR-6]; par-2(ok1723); unc-119(ed3)]*. J. Nance (New York University, New York, NY) provided a strain containing *zuIs151[nmy-2::mCherry]*. Knudra Transgenics generated strain COP1292 *knuSi719[pnu1134(sip-1p::plst-1(isoform a) with syntron::eGFP::tbb-2 UTR, unc-119(+)); unc-119(ed3) III]*. All strains used in this study are listed in Table S1.

CRISPR/Cas9 *plst-1* GFP knock-in transgenic worm generation

For CRISPR/Cas9 genome editing, we followed established protocols (Dickinson et al., 2013). The CRISPR targeting site 5′-GGACGATTT TCAGAGCTTTTCGG-3′ located in the last intron, 138 bp upstream of the C terminus of *plst-1*, was chosen using the online tool http:// crispr.mit.edu (Hsu et al., 2013). The CRISPR targeting site, with the exclusion of the PAM, was inserted into pDD162 (#47549; Addgene) using Phusion High-Fidelity DNA Polymerase (New England Biolabs, Inc.). The homologous repair template was generated by cloning 4,243 bp genomic DNA centered approximately on the C terminus of *plst-1* into pJET1.2/blunt vector using the CloneJET PCR Cloning kit (Thermo Fisher Scientific). A full-length GFP fragment with an N terminus 30-bp linker from pPD95.75 (#1494; Addgene) was then subsequently cloned into the pJET1.2 at the C terminus of *plst-1*, and the *plst-1* stop codon was simultaneously removed using the Gibson Assembly Cloning kit (New England Biolabs, Inc.). The PAM in the homologous repair template was mutated from 5′-NGG to 5′-NTT to block undesired cleavage by Cas9.

The modified pDD162, pJET1.2 containing homologous repair template, and an injection marker pRF4 *[rol-6(su1006)]* were then mixed at the concentration of 50 ng/µl each, respectively, and subsequently injected into the gonads of young adult hermaphrodites (Kim et al., 2014). Among 221 F1 rollers that were then screened visually using fluorescence wide-field microscope (Nikon) for GFP fluorescence, only one heterozygous GFP knock-in animal was identified. Knock-in was confirmed using PCR, and homozygous progeny were outcrossed to wild type four times before analysis was conducted. The GFP knock-in strain was subsequently verified via RNAi of GFP and *plst-1*, which resulted in the loss-of-contractility phenotype and the loss of GFP signal, respectively. It was also verified that the GFP insertion into the C terminus of *plst-1* did not result in any increase of embryonic lethality compared with the wild type.

Protein expression and purification

The *plst-1* isoform a cDNA was first amplified using Phusion High-Fidelity DNA Polymerase (New England Biolabs, Inc.) and inserted into a pET-based expression vector pSY5 (EMD Millipore), which encodes an 8× histidine tag at the N terminus, using Gibson Assembly Cloning kit (New England Biolabs, Inc.). pSY5 (plst-1 isoform a) was

sequenced to confirm fidelity of PCR amplification and in-frame insertion. The modified vector was then transformed into *E. coli* strain BL21, and a starter culture was grown to an optical density of 0.6 (OD 600 nm). The starter culture was then transferred into autoinduction medium grown at 15°C for 16 h. The bacterial culture was then lysed and purified using HisTrap FF affinity column (GE Healthcare) and cleaned up with size-exclusion chromatography using Superdex 200 (GE Healthcare). The recombinant protein was then eluted with 50 mM Tris, pH 8, 150 mM NaCl, concentrated to 9.5 mg/ml, and subsequently snap frozen in aliquots before subsequent use. SDS-PAGE and Coomassie blue staining confirmed the protein of the correct size and >90% purity. The protein band from the protein gel was then excised and sent for mass spectrometric analysis (Nanyang Technological University, Singapore) for protein identity confirmation.

F-actin cosedimentation assay

F-actin cosedimentation assay was performed using the Actin Binding Protein Biochem kit (Cytoskeleton, Inc.). In brief, rabbit muscle actin was polymerized for 1 h at room temperature from 21 µM Mg-ATP-actin monomers and incubated with PLST-1, BSA, or α-actinin (latter two for controls in low speed) at room temperature for 30 min and then spun at either 150,000 g (high speed) or 14,000 g (low speed) for 30 min. Equal volumes of supernatant and pellet were separated using 8–16% Mini-PROTEAN TGX Gels (Bio-Rad), stained with Coomassie blue for 30 min, and destained overnight. Protein gels were analyzed using ChemiDoc MP System (Bio-Rad).

RNAi

RNAi to knock down gene expression in worms was performed via feeding as previously described (Timmons, 2006). In brief, RNAi feeding clones were inoculated in LB broth supplemented with 100 µg/ml ampicillin for 16 h at 37°C. 50–200 µl of the overnight culture was then seeded on nematode growth medium plates supplemented with 100 µg/ml carbenicillin and 1 mM IPTG. The plates were allowed to dry at room temperature for 2 h and subsequently incubated at 37°C overnight. L4 larvae were transferred to these plates and incubated at 20°C for 36 h before being dissected for zygote collection.

When available, RNAi feeding clones were obtained from the Ahringer (Source BioScience) or Vidal (GE Healthcare) RNAi libraries (Kamath and Ahringer, 2003; Rual et al., 2004). Although *plst-1* RNAi feeding clone (Y104H12B_374.a) was available from the Ahringer RNAi library, there was unspecific targeting caused by 46% overlap with the *Y73B3B.1* full-length sequence. To circumvent this, a 608-bp cDNA fragment specific to *plst-1* only was cloned between SacI and KpnI in the multiple cloning site of the L4440 vector using standard cloning techniques and transformed into *E. coli* strain HT115. Primer pairs and template DNA for each gene are indicated in Table S2.

Confocal fluorescence microscopy

To obtain time-lapse or still fluorescence images of newly fertilized zygotes, gravid hermaphrodites were dissected in M9 buffer. The newly fertilized zygote was then transferred onto a 3% agarose pad using a mouth pipette and covered with a 22 × 22 mm cover glass. For whole-worm imaging in Fig. S2 B, a gravid hermaphrodite was anesthetized using 5 µl of 10 mM sodium azide for 10 min on a 3% agarose pad before being covered with a 22 × 22 mm cover glass. An additional 60 µl of M9 buffer was pipetted to the periphery of the agarose pad to prevent sample desiccation during image acquisition. Image acquisition was performed at 20°C on Ti-Eclipse inverted micro scope (Nikon) equipped with CSU-X1 spinning disk confocal head (Yokogawa Electric Corporation), DPSS-Laser (Roper Technologies) of 491 and 568 nm excitation wavelengths, and an Evolve Rapid-Cal

electron multiplying charged-coupled device camera (Photometrics). Focus drift during time-lapse acquisition was corrected using Perfect Focus System (Nikon). Acquisition control was performed using Meta-Morph (Molecular Devices). All image acquisition of the zygote was performed with a 100× 1.4 NA oil-immersion Plan-Apochromat objective (Nikon, Japan) with 1 × 1 binning with the exception of acquisition of zygotes coexpressing GFP::PLC1δ-PH and HIS-58::mCherry (Fig. 3 C and Fig. 6 A), where a 2 × 2 binning was used instead. For whole-worm image acquisition in Fig. S2 B, a 60× 1.4 NA oil-immersion Plan-Apochromat objective (Nikon) with 1 × 1 binning was used.

Image analysis

Fiji (Schindelin et al., 2012), MetaMorph (Molecular Devices), and MATLAB (MathWorks) were used to perform image processing and quantitative analysis. All images were corrected for bleaching and background noise before further quantitative analysis. Pearson's correlation coefficient between PLST-1::GFP and Lifeact::RFP was quantified using the Coloc 2 plugin (http://imagej.net/Coloc_2) in Fiji. Ratiometric GFP/RFP images in Fig. 1 (D and E) were made using the Ratio Plus plugin (http://rsb.info.nih.gov/ij/plugins/ratio-plus.html) and pseudocolored using the NucMed plugin (http://www.med.harvard.edu/JPNM/ij/plugins/NucMed.html). Mature cortical NMY-2 focus area in Fig. 4 D was measured by manual tracing. The movie of each NMY-2 focus area was played backward to earliest possible frame where nascent NMY-2 filaments were about to undergo coalescence and the outermost NMY-2 filaments were then traced manually to form a perimeter and the area was measured for Fig. 4 C. NMY-2 focus lifetime in Fig. 4 E was measured by applying an intensity threshold and subsequently using the MTrack2 plugin (http://valelab.ucsf.edu/~nstuurman/IJplugins/MTrack2.html).

For quantitative analysis in Figs. 5 (B–E), S5 (D–G), and S6 (A–D), a 256 × 128 pixel (40.96 × 20.48 µm) region of interest was applied to all zygotes to standardize the cortex area. The zygote-to-zygote cortical area difference is especially prominent in wild-type zygotes, where cortical rufflings result in the periphery of the cortex to be out of focus. To quantify the cortical flow vector field in Figs. 5 (C and D), S5 (E and F), and S6 (B–D), iterative PIV analysis was performed using the PIV plugin (https://sites.google.com/site/qingzongtseng/piv).

The cosine similarity profiles in Figs. 5 (D and E), S5 (F and G), and S6 F were measured using a custom MATLAB algorithm. In brief, the cosine similarity for each pair of velocity vector is defined as the cosine of the angle subtended by the two vectors, that is,

$$\cos\_\mathrm{sim}(\vec{v_1}, \vec{v_2}) = \frac{\vec{v_1} \cdot \vec{v_2}}{\| \vec{v_1} \| \cdot \| \vec{v_2} \|}.$$

The cosine similarity ranges from −1 to 1, the larger the value is, the higher the directional similarity of the two velocity vectors. For each image stack, the cosine similarity for all vector pairs with separation distance, r was averaged to get the mean velocity correlation for each discrete distance r. The mean cosine similarity was plotted as a function of r to demonstrate the relation between cosine similarity and separation distance.

To analyze the distribution of mCherry::PAR-6 and GFP::PAR-2 fluorescent intensity along the plasma membrane in Fig. 5 (F and G), an in-house MATLAB code was used for segmenting the membrane, generating the kymograph and computing the intensity ratio. First, the mCherry images and GFP images were background subtracted and rotated to the same orientation. Next, each pair of mCherry image and GFP image was combined to generate a binary mask using local Otsu thresholding. A 5-pixel-width boundary was then extracted from the binary mask, and the pixels along this boundary were represented by their angular position, where 0° denotes the anterior and 180° denotes

the posterior. With this, a kymograph of boundary intensity was generated in which the x axis represents the angular position and the y axis represents time (Fig. 5 G). To quantify the mCherry::PAR-6 and the GFP::PAR-2 polarity indices, respectively, in Fig. 5 H, the plasma membrane was divided into two equal halves, where pixels with angular position from 90° to 270° belong to the posterior half and the remaining pixels belong to the anterior half. The polarity index for mCherry::PAR-6 is thus calculated as the ratio of the mCherry::PAR-6 fluorescence intensity of the anterior half boundary and mCherry::PAR-6 fluorescence intensity along the whole boundary. Likewise, the polarity index for GFP::PAR-2 is thus calculated as the ratio of the GFP::PAR-2 fluorescence intensity of the posterior half boundary and GFP::PAR-2 fluorescence intensity along the whole boundary.

For Figs. 6 (E and F) and S6 (A–C), the 256 × 128 pixel (40.96 × 20.48 µm) zygote cortex is subdivided into three regions for PIV analysis or fluorescence intensity measurement: anterior cortex (first to 128th pixel; 0.16–20.48 µm along the A-P axis), furrowing zone (129th–183rd pixel; 20.64–29.28 µm along the A-P axis), and posterior cortex (184th–256th pixel; 29.44–40.96 µm along the A-P axis).

Cortical laser ablation

The system of laser ablation was previously described (Kiehart et al., 2006; Hara et al., 2016). In brief, an ultraviolet laser (355 nm, 300 ps pulse duration, 1 kHz repetition rate, PowerChip PNV-0150-100, team photonics) were interfaced to the Nikon A1R MP confocal microscope. The UV laser was integrated into a Nikon ECLIPSE Ti microscope through a customized optical path and a customized dichroic filter and coaligned with the optical axis of the microscope. The position of the laser was controlled by a mirror mounted on two linear actuators (TRA12CC; Newport), and the exposure time of the laser was controlled by a mechanical shutter (VS25S2ZM0; Uniblitz). The actuators (through the actuator controller, ESP301-3G; Newport) and shutter were controlled by custom ImageJ plug-ins from a PC. The laser ablation system, which is independent from imaging microscope, allows us to perform an ablation during imaging.

We conducted laser ablations as previously described (Mayer et al., 2010). Specifically, we applied 50 ultraviolet pulses to each five equidistant sites along a 6-µm line, which was controlled by an ImageJ plug-in. The laser ablations were performed when the anterior myosin-rich cortex occupied 70% of the embryo length. An ablation was performed at the plane of cortical myosin by the UV laser with the laser power of ~250 nW at back aperture of the objective. Images were acquired every 1.1 s. Imaging was started ~5 s before the ablation and finished ~1–2 min after the ablation.

The initial outward velocity was quantified by performing PIV analysis (http://www.mn.uio.no/math/english/people/aca/jks/matpiv/) on the precut and postcut frames. The outward velocity flow field was averaged in two 6.6 µm × 4.2 µm rectangular regions top and bottom relative to the ablation line, and the mean orthogonal component to the ablation site is the initial outward velocity.

Physical model of network

Computer simulations were performed with Cytosim, an Open Source project (http://github.com/nedelec/cytosim), following overdamped Langevin dynamics (Nédélec and Foethke, 2007). For this study, every network was composed of 5,000 filaments of length 2.2 µm and with a rigidity of 0.05 µm^2 pN. The motors and cross-linkers were composed of two identical subunits, linked by a stiffness of 250 pN/µm, diffusing at 10 µm^2/s. Both the motor and cross-linker subunits bind at a distance of 10 nm with a rate of 10 s^{-1} and unbinds with a constant rate of 0.5 s^{-1}. The motor obeys a linear force–velocity relationship with an unloaded speed of 0.5 µm/s and a stall force of 6 pN. The network

is initialized by distributing all the filaments randomly such that their center is within a disc of radius 10 µm. The system is simulated with a viscosity of 0.1 pN s µm^{-2}, a thermal energy of 0.0042 pN µm, and a time step of 1 ms, until 4 s of network time is reached.

Bioinformatics

Multiple sequence alignment was performed using T-Coffee (Notredame et al., 2000) and visualized using Jalview (Waterhouse et al., 2009). Sequence identities and similarities were calculated using SIAS (http://imed.med.ucm.es/Tools/sias.html).

Statistical analysis

Unpaired nonparametric test (Mann–Whitney U test) were conducted using Prism 6 (GraphPad Software).

Online supplemental material

Fig. S1 contains a multiple sequence alignment of *C. elegans* PLST-1 with other plastin/fimbrin orthologues. Fig. S2 shows the expression pattern of endogenous PLST-1::GFP during later embryogenesis and in the adult hermaphrodite. Fig. S3 shows the phenotypes of *plst-1* RNAi and the rescue of *plst-1(tm4255)* by expression of a PLST-1::GFP transgene. Fig. S4 demonstrates that α-actinin is not involved in the regulation of cortical contractility in the zygote. Fig. S5 contains analysis of cortical flows during polarity establishment and initiation of cytokinesis. Video 1 shows PLST-1::GFP and the F-actin reporter Lifeact::RFP in the cortex of the newly fertilized zygote. Video 2 is a ratiometric view of PLST-1::GFP and the F-actin reporter Lifeact::RFP in the cortex of the newly fertilized zygote. Video 3 shows an equatorial view of control and plst-1 zygotes expressing a membrane marker and histone marker from polarization to the completion of first cell division. Video 4 shows an equatorial view of control and *plst-1* zygotes expressing a membrane marker and GFP::tubulin during spindle oscillation. Video 5 follows a cortical laser ablation performed at the anterior cortex of control and *plst-1* zygotes expressing NMY-2::GFP. Video 6 shows a cortical view of control and *plst-1* zygotes expressing GFP::Utrophin during polarity establishment and polarity maintenance. Video 7 shows a cortical view of control and *plst-1* zygotes expressing NMY-2::mCherry during polarity establishment and polarity maintenance. Video 8 shows a cortical view of control and *plst-1* zygotes expressing GFP::Utrophin and NMY-2::mCherry immediately after separation of sister chromatids. Video 9 is an equatorial view of control and *plst-1* zygotes expressing mCherry::PAR-6 and GFP::PAR-2 from polarity establishment until completion of first cell division. Table S1 contains a list of strains used in this study with their genotypes. Table S2 contains a list of RNAi feeding clones used in this study.

References

Albertson, D.G. 1984. Formation of the first cleavage spindle in nematode embryos. *Dev. Biol.* 101:61–72. http://dx.doi.org/10.1016/0012-1606(84)90117-9

Behm-Ansmant, I., I. Kashima, J. Rehwinkel, J. Saulière, N. Wittkopp, and E. Izaurralde. 2007. mRNA quality control: An ancient machinery recognizes and degrades mRNAs with nonsense codons. *FEBS Lett.* 581:2845–2853. http://dx.doi.org/10.1016/j.febslet.2007.05.027

Bendix, P.M., G.H. Koenderink, D. Cuvelier, Z. Dogic, B.N. Koeleman, W.M. Brieher, C.M. Field, L. Mahadevan, and D.A. Weitz. 2008. A quantitative analysis of contractility in active cytoskeletal protein networks. *Biophys. J.* 94:3126–3136. http://dx.doi.org/10.1529/biophysj.107.117960

Brenner, S. 1974. The genetics of *Caenorhabditis elegans. Genetics.* 77:71–94.

Bretscher, A. 1981. Fimbrin is a cytoskeletal protein that crosslinks F-actin in vitro. *Proc. Natl. Acad. Sci. USA.* 78:6849–6853. http://dx.doi.org/10.1073/pnas.78.11.6849

Bretscher, A., and K. Weber. 1980. Fimbrin, a new microfilament-associated protein present in microvilli and other cell surface structures. *J. Cell Biol.* 86:335–340. http://dx.doi.org/10.1083/jcb.86.1.335

Chang, Y.-F., J.S. Imam, and M.F. Wilkinson. 2007. The nonsense-mediated decay RNA surveillance pathway. *Annu. Rev. Biochem.* 76:51–74. http://dx.doi.org/10.1146/annurev.biochem.76.050106.093909

de Arruda, M.V., S. Watson, C.S. Lin, J. Leavitt, and P. Matsudaira. 1990. Fimbrin is a homologue of the cytoplasmic phosphoprotein plastin and has domains homologous with calmodulin and actin gelation proteins. *J. Cell Biol.* 111:1069–1079. http://dx.doi.org/10.1083/jcb.111.3.1069

Delanote, V., J. Vandekerckhove, and J. Gettemans. 2005. Plastins: Versatile modulators of actin organization in (patho)physiological cellular processes. *Acta Pharmacol. Sin.* 26:769–779. http://dx.doi.org/10.1111/j.1745-7254.2005.00145.x

Dickinson, D.J., J.D. Ward, D.J. Reiner, and B. Goldstein. 2013. Engineering the *Caenorhabditis elegans* genome using Cas9-triggered homologous recombination. *Nat. Methods.* 10:1028–1034. http://dx.doi.org/10.1038/nmeth.2641

Dimitriadi, M., J.N. Sleigh, A. Walker, H.C. Chang, A. Sen, G. Kalloo, J. Harris, T. Barsby, M.B. Walsh, J.S. Satterlee, et al. 2010. Conserved genes act as modifiers of invertebrate SMN loss of function defects. *PLoS Genet.* 6:e1001172. http://dx.doi.org/10.1371/journal.pgen.1001172

Ennomani, H., G. Letort, C. Guérin, J.-L. Martiel, W. Cao, F. Nédélec, E.M. De La Cruz, M. Théry, and L. Blanchoin. 2016. Architecture and connectivity govern actin network contractility. *Curr. Biol.* 26:616–626. http://dx.doi.org/10.1016/j.cub.2015.12.069

Ezzell, R.M., M.M. Chafel, and P.T. Matsudaira. 1989. Differential localization of villin and fimbrin during development of the mouse visceral endoderm and intestinal epithelium. *Development.* 106:407–419.

Fievet, B.T., J. Rodriguez, S. Naganathan, C. Lee, E. Zeiser, T. Ishidate, M. Shirayama, S. Grill, and J. Ahringer. 2013. Systematic genetic interaction screens uncover cell polarity regulators and functional redundancy. *Nat. Cell Biol.* 15:103–112. http://dx.doi.org/10.1038/ncb2639

Flock, A., A. Bretscher, and K. Weber. 1982. Immunohistochemical localization of several cytoskeletal proteins in inner ear sensory and supporting cells. *Hear. Res.* 7:75–89. http://dx.doi.org/10.1016/0378-5955(82)90082-X

Freeley, M., F. O'Dowd, T. Paul, D. Kashanin, A. Davies, D. Kelleher, and A. Long. 2012. L-plastin regulates polarization and migration in chemokine-stimulated human T lymphocytes. *J. Immunol.* 188:6357–6370. http://dx.doi.org/10.4049/jimmunol.1103242

Gardel, M.L., J.H. Shin, F.C. MacKintosh, L. Mahadevan, P. Matsudaira, and D.A. Weitz. 2004. Elastic behavior of cross-linked and bundled actin networks. *Science.* 304:1301–1305. http://dx.doi.org/10.1126/science.1095087

Glenney, J.R.J. Jr., P. Kaulfus, P. Matsudaira, and K. Weber. 1981. F-actin binding and bundling properties of fimbrin, a major cytoskeletal protein of microvillus core filaments. *J. Biol. Chem.* 256:9283–9288.

Hara, Y., M. Shagirov, and Y. Toyama. 2016. Cell boundary elongation by non-autonomous contractility in cell oscillation. *Curr. Biol.* 26:2388–2396. http://dx.doi.org/10.1016/j.cub.2016.07.003

Hill, D.P., and S. Strome. 1988. An analysis of the role of microfilaments in the establishment and maintenance of asymmetry in *Caenorhabditis elegans* zygotes. *Dev. Biol.* 125:75–84. http://dx.doi.org/10.1016/0012-1606(88)90060-7

Hird, S.N., and J.G. White. 1993. Cortical and cytoplasmic flow polarity in early embryonic cells of *Caenorhabditis elegans*. *J. Cell Biol.* 121:1343–1355. http://dx.doi.org/10.1083/jcb.121.6.1343

Hsu, P.D., D.A. Scott, J.A. Weinstein, F.A. Ran, S. Konermann, V. Agarwala, Y. Li, E.J. Fine, X. Wu, O. Shalem, et al. 2013. DNA targeting specificity of RNA-guided Cas9 nucleases. *Nat. Biotechnol.* 31:827–832. http://dx.doi.org/10.1038/nbt.2647

Janson, L.W., J. Kolega, and D.L. Taylor. 1991. Modulation of contraction by gelation/solation in a reconstituted motile model. *J. Cell Biol.* 114:1005–1015. http://dx.doi.org/10.1083/jcb.114.5.1005

Kamath, R.S., and J. Ahringer. 2003. Genome-wide RNAi screening in *Caenorhabditis elegans*. *Methods.* 30:313–321. http://dx.doi.org/10.1016/S1046-2023(03)00050-1

Kiehart, D.P., Y. Tokutake, C. Chang, M. Hutson, J. Wiemann, X. Peralta, Y. Toyama, A. Wells, A. Rodriguez, and G. Edwards. 2006. Ultraviolet laser microbeam for dissection of drosophila embryos. *In* Cell Biology. Third edition. J.E. Celis, editor. Academic Press, San Diego/London. 87–103. http://dx.doi.org/10.1016/B978-012164730-8/50137-4

Kim, H., T. Ishidate, K.S. Ghanta, M. Seth, D. Conte Jr., M. Shirayama, and C.C. Mello. 2014. A co-CRISPR strategy for efficient genome editing in *Caenorhabditis elegans*. *Genetics.* 197:1069–1080. http://dx.doi.org/10.1534/genetics.114.166389

Krey, J.F., E.S. Krystofiak, R.A. Dumont, S. Vijayakumar, D. Choi, F. Rivero, B. Kachar, S.M. Jones, and P.G. Barr-Gillespie. 2016. Plastin 1 widens stereocilia by transforming actin filament packing from hexagonal to liquid. *J. Cell Biol.* 215:467–482. http://dx.doi.org/10.1083/jcb.201606036

Laporte, D., N. Ojkic, D. Vavylonis, and J.-Q. Wu. 2012. α-Actinin and fimbrin cooperate with myosin II to organize actomyosin bundles during contractile-ring assembly. *Mol. Biol. Cell.* 23:3094–3110. http://dx.doi.org/10.1091/mbc.E12-02-0123

Lecuit, T., and P.-F. Lenne. 2007. Cell surface mechanics and the control of cell shape, tissue patterns and morphogenesis. *Nat. Rev. Mol. Cell Biol.* 8:633–644. http://dx.doi.org/10.1038/nrm2222

Levayer, R., and T. Lecuit. 2012. Biomechanical regulation of contractility: Spatial control and dynamics. *Trends Cell Biol.* 22:61–81. http://dx.doi.org/10.1016/j.tcb.2011.10.001

Lewellyn, L., A. Carvalho, A. Desai, A.S. Maddox, and K. Oegema. 2011. The chromosomal passenger complex and centralspindlin independently contribute to contractile ring assembly. *J. Cell Biol.* 193:155–169. http://dx.doi.org/10.1083/jcb.201008138

Lin, C.-S., T. Park, Z.P. Chen, and J. Leavitt. 1993. Human plastin genes. Comparative gene structure, chromosome location, and differential expression in normal and neoplastic cells. *J. Biol. Chem.* 268:2781–2792.

Maddox, A.S., B. Habermann, A. Desai, and K. Oegema. 2005. Distinct roles for two C. elegans anillins in the gonad and early embryo. *Development.* 132:2837–2848. http://dx.doi.org/10.1242/dev.01828

Matsudaira, P., E. Mandelkow, W. Renner, L.K. Hesterberg, and K. Weber. 1983. Role of fimbrin and villin in determining the interfilament distances of actin bundles. *Nature.* 301:209–214. http://dx.doi.org/10.1038/301209a0

Mayer, M., M. Depken, J.S. Bois, F. Jülicher, and S.W. Grill. 2010. Anisotropies in cortical tension reveal the physical basis of polarizing cortical flows. *Nature.* 467:617–621. http://dx.doi.org/10.1038/nature09376

Messier, J.M., L.M. Shaw, M. Chafel, P. Matsudaira, and A.M. Mercurio. 1993. Fimbrin localized to an insoluble cytoskeletal fraction is constitutively phosphorylated on its headpiece domain in adherent macrophages. *Cell Motil. Cytoskeleton.* 25:223–233. http://dx.doi.org/10.1002/cm.970250303

Meyer, R.K., and U. Aebi. 1990. Bundling of actin filaments by alpha-actinin depends on its molecular length. *J. Cell Biol.* 110:2013–2024. http://dx.doi.org/10.1083/jcb.110.6.2013

Moulder, G.L., G.H. Cremona, J. Duerr, J.N. Stirman, S.D. Fields, W. Martin, H. Qadota, G.M. Benian, H. Lu, and R.J. Barstead. 2010. α-Actinin is required for the proper assembly of Z-disk/focal-adhesion-like structures and for efficient locomotion in Caenorhabditis elegans. *J. Mol. Biol.* 403:516–528. http://dx.doi.org/10.1016/j.jmb.2010.08.055

Munjal, A., and T. Lecuit. 2014. Actomyosin networks and tissue morphogenesis. *Development.* 141:1789–1793. http://dx.doi.org/10.1242/dev.091645

Munro, E., J. Nance, and J.R. Priess. 2004. Cortical flows powered by asymmetrical contraction transport PAR proteins to establish and maintain anterior-posterior polarity in the early *C. elegans* embryo. *Dev. Cell.* 7:413–424. http://dx.doi.org/10.1016/j.devcel.2004.08.001

Murrell, M.P., and M.L. Gardel. 2012. F-actin buckling coordinates contractility and severing in a biomimetic actomyosin cortex. *Proc. Natl. Acad. Sci. USA.* 109:20820–20825. http://dx.doi.org/10.1073/pnas.1214753109

Naganathan, S.R., S. Fürthauer, M. Nishikawa, F. Jülicher, and S.W. Grill. 2014. Active torque generation by the actomyosin cell cortex drives left-right symmetry breaking. *eLife.* 3:e04165. http://dx.doi.org/10.7554/eLife.04165

Nakano, K., K. Satoh, A. Morimatsu, M. Ohnuma, and I. Mabuchi. 2001. Interactions among a fimbrin, a capping protein, and an actin-depolymerizing factor in organization of the fission yeast actin cytoskeleton. *Mol. Biol. Cell.* 12:3515–3526. http://dx.doi.org/10.1091/mbc.12.11.3515

Nédélec, F., and D. Foethke. 2007. Collective Langevin dynamics of flexible cytoskeletal fibers. *New J. Phys.* 9:427. http://dx.doi.org/10.1088/1367-2630/9/11/427

Notredame, C., D.G. Higgins, and J. Heringa. 2000. T-Coffee: A novel method for fast and accurate multiple sequence alignment. *J. Mol. Biol.* 302:205–217. http://dx.doi.org/10.1006/jmbi.2000.4042

Padmanabhan, A., H.T. Ong, and R. Zaidel-Bar. 2017. Non-junctional E-cadherin clusters regulate the actomyosin cortex in the *C. elegans* zygote. *Curr. Biol.* 27:103–112. http://dx.doi.org/10.1016/j.cub.2016.10.032

Prassler, J., S. Stocker, G. Marriott, M. Heidecker, J. Kellermann, and G. Gerisch. 1997. Interaction of a Dictyostelium member of the plastin/fimbrin family with actin filaments and actin-myosin complexes. *Mol. Biol. Cell.* 8:83–95. http://dx.doi.org/10.1091/mbc.8.1.83

Redemann, S., J. Pecreaux, N.W. Goehring, K. Khairy, E.H.K. Stelzer, A.A. Hyman, and J. Howard. 2010. Membrane invaginations reveal cortical sites that pull on mitotic spindles in one-cell *C. elegans* embryos. *PLoS One.* 5:e12301. http://dx.doi.org/10.1371/journal.pone.0012301

Reichl, E.M., Y. Ren, M.K. Morphew, M. Delannoy, J.C. Effler, K.D. Girard, S. Divi, P.A. Iglesias, S.C. Kuo, and D.N. Robinson. 2008. Interactions between myosin and actin crosslinkers control cytokinesis contractility dynamics and mechanics. *Curr. Biol.* 18:471–480. http://dx.doi.org/10.1016/j.cub.2008.02.056

Rual, J.-F., J. Ceron, J. Koreth, T. Hao, A.-S. Nicot, T. Hirozane-Kishikawa, J. Vandenhaute, S.H. Orkin, D.E. Hill, S. van den Heuvel, and M. Vidal. 2004. Toward improving *Caenorhabditis elegans* phenome mapping with an ORFeome-based RNAi library. *Genome Res.* 14:2162–2168. http://dx.doi.org/10.1101/gr.2505604

Salbreux, G., G. Charras, and E. Paluch. 2012. Actin cortex mechanics and cellular morphogenesis. *Trends Cell Biol.* 22:536–545. http://dx.doi.org/10.1016/j.tcb.2012.07.001

Schindelin, J., I. Arganda-Carreras, E. Frise, V. Kaynig, M. Longair, T. Pietzsch, S. Preibisch, C. Rueden, S. Saalfeld, B. Schmid, et al. 2012. Fiji: An open-source platform for biological-image analysis. *Nat. Methods.* 9:676–682. http://dx.doi.org/10.1038/nmeth.2019

Schonegg, S., A.A. Hyman, and W.B. Wood. 2014. Timing and mechanism of the initial cue establishing handed left–right asymmetry in *Caenorhabditis elegans* embryos. *Genesis.* 52:572–580. http://dx.doi.org/10.1002/dvg.22749

Shirayama, S., and O. Numata. 2003. Tetrahymena fimbrin localized in the division furrow bundles actin filaments in a calcium-independent manner. *J. Biochem.* 134:591–598. http://dx.doi.org/10.1093/jb/mvg183

Shivas, J.M., and A.R. Skop. 2012. Arp2/3 mediates early endosome dynamics necessary for the maintenance of PAR asymmetry in *Caenorhabditis elegans*. *Mol. Biol. Cell.* 23:1917–1927. http://dx.doi.org/10.1091/mbc.E12-01-0006

Singh, D., and C. Pohl. 2014. Coupling of rotational cortical flow, asymmetric midbody positioning, and spindle rotation mediates dorsoventral axis formation in *C. elegans*. *Dev. Cell.* 28:253–267. http://dx.doi.org/10.1016/j.devcel.2014.01.002

Skau, C.T., D.S. Courson, A.J. Bestul, J.D. Winkelman, R.S. Rock, V. Sirotkin, and D.R. Kovar. 2011. Actin filament bundling by fimbrin is important for endocytosis, cytokinesis, and polarization in fission yeast. *J. Biol. Chem.* 286:26964–26977. http://dx.doi.org/10.1074/jbc.M111.239004

Skop, A.R., H. Liu, J. Yates III, B.J. Meyer, and R. Heald. 2004. Dissection of the mammalian midbody proteome reveals conserved cytokinesis mechanisms. *Science.* 305:61–66. http://dx.doi.org/10.1126/science.1097931

Stossel, T.P., G. Fenteany, and J.H. Hartwig. 2006. Cell surface actin remodeling. *J. Cell Sci.* 119:3261–3264. http://dx.doi.org/10.1242/jcs.02994

Strome, S. 1986. Fluorescence visualization of the distribution of microfilaments in gonads and early embryos of the nematode *Caenorhabditis elegans*. *J. Cell Biol.* 103:2241–2252. http://dx.doi.org/10.1083/jcb.103.6.2241

Strome, S., and W.B. Wood. 1983. Generation of asymmetry and segregation of germ-line granules in early *C. elegans* embryos. *Cell.* 35:15–25. http://dx.doi.org/10.1016/0092-8674(83)90203-9

Timmons, L. 2006. Delivery methods for RNA interference in *C. elegans*. In C. elegans: Methods and Applications. Vol. 351. K. Strange, editor. Humana Press, New York. 119–125.

Tse, Y.C., A. Piekny, and M. Glotzer. 2011. Anillin promotes astral microtubule-directed cortical myosin polarization. *Mol. Biol. Cell.* 22:3165–3175. http://dx.doi.org/10.1091/mbc.E11-05-0399

Velarde, N., K.C. Gunsalus, and F. Piano. 2007. Diverse roles of actin in *C. elegans* early embryogenesis. *BMC Dev. Biol.* 7:142. http://dx.doi.org/10.1186/1471-213X-7-142

Wabnitz, G.H., P. Lohneis, H. Kirchgessner, B. Jahraus, S. Gottwald, M. Konstandin, M. Klemke, and Y. Samstag. 2010. Sustained LFA-1 cluster formation in the immune synapse requires the combined activities of L-plastin and calmodulin. *Eur. J. Immunol.* 40:2437–2449. http://dx.doi.org/10.1002/eji.201040345

Wachsstock, D.H., W.H. Schwarz, and T.D. Pollard. 1994. Cross-linker dynamics determine the mechanical properties of actin gels. *Biophys. J.* 66:801–809. http://dx.doi.org/10.1016/S0006-3495(94)80856-2

Wagner, B., R. Tharmann, I. Haase, M. Fischer, and A.R. Bausch. 2006. Cytoskeletal polymer networks: the molecular structure of cross-linkers determines macroscopic properties. *Proc. Natl. Acad. Sci. USA.* 103:13974–13978. http://dx.doi.org/10.1073/pnas.0510190103

Waterhouse, A.M., J.B. Procter, D.M.A. Martin, M. Clamp, and G.J. Barton. 2009. Jalview Version 2: A multiple sequence alignment editor and analysis workbench. *Bioinformatics.* 25:1189–1191. http://dx.doi.org/10.1093/bioinformatics/btp033

Werner, M., E. Munro, and M. Glotzer. 2007. Astral signals spatially bias cortical myosin recruitment to break symmetry and promote cytokinesis. *Curr. Biol.* 17:1286–1297. http://dx.doi.org/10.1016/j.cub.2007.06.070

Xu, J., D. Wirtz, and T.D. Pollard. 1998. Dynamic cross-linking by alpha-actinin determines the mechanical properties of actin filament networks. *J. Biol. Chem.* 273:9570–9576. http://dx.doi.org/10.1074/jbc.273.16.9570

Zaidel-Bar, R., G. Zhenhuan, and C. Luxenburg. 2015. The contractome: A systems view of actomyosin contractility in non-muscle cells. *J. Cell Sci.* 128:2209–2217. http://dx.doi.org/10.1242/jcs.170068